



Study of the interlaminar fracture under mode I loading on FFF printed parts

J. Fonseca^a, I.A. Ferreira^{a,b,*}, M.F.S.F. de Moura^{a,b}, M. Machado^b, J.L. Alves^{a,b}

^a Department of Mechanical Engineering, Faculty of Engineering, University of Porto, Porto, Portugal

^b INEGI, Porto, Portugal

ARTICLE INFO

Keywords:

FFF
Fracture
Interlaminar strength
Delamination
AM
Mode I fracture

ABSTRACT

The present study aims the development of a methodology for the analysis and evaluation of the fracture toughness under mode I loading of 3D printed parts, produced by the fused filament fabrication (FFF) additive technology. This work is motivated by the urgent need of improvement in this area, in order to extend the reliability of this process to applications which require high mechanical performance. For this purpose, a specific geometry was developed, taking into account the inherent characteristics of both, the applied material and process used for the production of double cantilever beam (DCB) tests. A set of experimental tests was performed with pure and short fibre reinforced Polyamide 12 (PA 12), and, in parallel, a numerical analysis was also followed for each series. Posteriorly, an inspection on the fracture surfaces was made, by microscopy, in order to refine the conclusions obtained and furtherly comprehend the variables in play. The obtained results provided a consistent value for the fracture toughness for only one of the cases studied, being this the unreinforced material. However, for the reinforced material, a set of conclusions which justify its behaviour was also able to be attained. The followed approach for the numerical analysis also revealed to be as suitable for this specific combination of material and additive process.

1. Introduction

Fused Filament Fabrication (FFF) is one of the most popular additive manufacturing (AM) techniques, which has been regarded as an effective method for the creation of complex geometries. However, as it can be understood from the production process, which rely on creating the desired geometry layer by layer, the interfacial bonding strength between the mentioned layers plays an important role on the mechanical properties of the resulting part. Since each layer is created by deposition of a line of extruded filament in a defined orientation, this process is also prone to induce manufacturing defects, such as voids or air gaps. In fact, one of the major issues when applying this technique is the highly anisotropic behaviour exhibited by the produced parts, which is undesirable when the demanded application requires a high mechanical performance. This effect is considered to be one of the major limitations in the current state of art for FFF process, since it limits its applicability to aesthetic and low load bearing components. The type of tests developed in this work, consider two different of feedstock materials. A pure PA 12 and a reinforced version of the same material were used for sample production, introducing the fibres as another variable process uncertainty. As it can be perceived by this conclusion, it is important to develop solutions from which higher mechanical properties can be

obtained, in order to increase its viability for this type of applications.

Thus far, conducted researches are primarily focused in the mechanical performance identification by associating the feedstock material, the process and the type of printing settings that are used. The influence of correct parametrization of FFF printed parts is key in defining how capable is the mechanical response, when submitted to a solicitation. Studied parameters are mainly defined by three categories (Fig. 1): material-related for printing temperatures; geometric-related, with properties like infill orientation/width, air gap and layer height, and process-related, for printing speeds, extrusion flow among others. Those also define the level of anisotropy taking into account the part orientation when printed [1–4]. Most of these studies focuses in tensile properties of printed parts, leaving a characterization gap when considering the interlayer mechanical performance.

Other resultant property is the dimensional accuracy. Studies show the influence of these parametrization on the definition of how exact or not the initial CAD geometry can become after printing [5]. It was proven that parameter such as extrusion multiplier is one of the most responsible factors for distortions in the printed sample [6]. In a similar set of experiments, [7] proved that raster width and thickness were the most influential factors when considering dimensional accuracy [8–10].

Regarding fracture toughness, few studies have been conducted. In

* Corresponding author at: Department of Mechanical Engineering, Faculty of Engineering, University of Porto, Porto, Portugal.

E-mail address: iaferreira@inegi.up.pt (I.A. Ferreira).

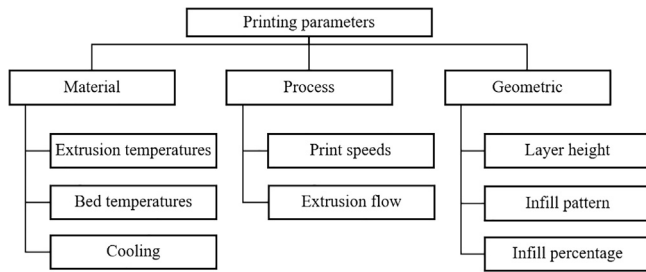


Fig. 1. Printing parameters division.

[8] research, a modified DCB sample, version of the ASTM D5528 is applied for the experimental tests, followed by the use of the Compliance Calibration Method (CCM) data reduction scheme. The authors concluded that this standard is an adequate methodology for the characterization of the interlayer performance of FFF components, filling in part of the existent characterization gap, which may prove essential for the development of the technology. Furtherly sustaining this conclusion, a study presented in [9] attempted to characterize the fracture behaviour of DCB specimens created with Acrylonitrile butadiene styrene (ABS), employing cohesive damage models. The authors concluded that this type of approach can be used as an effective tool to capture the interlayer fracture behaviour of the FFF components, as well as to improve the fracture energy estimation procedure of the final components. In [10], a DCB test is conducted on samples manufactured with Polylactic acid (PLA) supplied by Prirevo e.U., Austria. It was concluded that the layer design parameters, such as layer thickness or raster orientation specific for the type of load applied, are key aspects in enhancing the interlaminar strength of the final component. It was also stated that the DCB test is an appropriate methodology to perform studies for this type of technology.

Due to being created with a layer by layer step process, the parts obtained from the FFF technology can be regarded in the same light as laminate composites. As result, they tend to exhibit the same type of problems as these composites. Among them, the possible delamination effect between adjacent layers is one of the most severe types of damage that can occur, being its consequence a reduction on the mechanical properties, resulting in an early failure of the component [11]. This effect is due to a crack propagation phenomenon, which is a typical application of the fracture mechanics concepts. The same problems are susceptible to occur between adjacent layers of the FFF components, since the process itself is responsible for the separation of the layers.

Taking into account the previously mentioned discussion, this work intends to study the bond connection between layers, i.e., the interlaminar strength and toughness under mode I loading at these critical interfaces, of components created by the FFF process. In order to do this, an analysis via fracture mechanics concepts will be applied, for the characterization of the crack propagation behaviour presented by a series of experimental tests. This is done in order to study and adequate a method from which the correct measurement of the fracture toughness can be obtained. By using a test geometry based on the DCB test, portrayed by ASTM D5528 standard for unidirectional fibre reinforced polymer matrix composites [12], a methodology for sample creation was developed avoiding the usage of reinforcing doublers. The aim is to present measures that can be taken to enhance it, since it is the main property responsible for characterization of the fracture between layers. As stated previously, this work presents a newly developed approach to fracture toughness under mode I, by defining a new test geometry, including an also printed disposable supporting structure that allows for a more accurate pre-crack creation, using reinforced and unreinforced FFF printed PA 12 parts, in parallel with numerical simulations for result validation.

2. Materials and methods

2.1. Material selection

Two types of 1.75 mm diameter PA 12 from Fillamentum ©, Parzlich s.r.o (Czech Republic) materials were selected. A pure version of PA 12 (Nylon FX 256) and a composite one (CF15), reinforced by short carbon fibres (15 vol.%), with approximately 100 µm in length and 10 µm diameter, both obtained in filament form. This selection was made based on research requirements in this area, which is the implementation of reinforced composites in the FFF process [13,11]. This type of polymer is widely regarded as an engineering plastic, being suitable for applications which require load bearing. The interest in applying this material to the FFF technology is understood as a need for further advancement in the mechanical properties, which are able to be obtained from it. Furthermore, the same type of investigations is also currently being conducted for other polymers, for instance ABS [14,15] and PLA [16]. However few studies have been conducted with engineering thermoplastic such as PA 12, which reinforces the appropriateness of searching a suitable testing methodology.

2.2. Development and fabrication of DCB printed samples

2.2.1. Definition of DCB overall dimensions

As a first approach, the specimen dimension procedure applied in [8] was considered. Those authors decided, due to the low stiffness of the material (ABS), to apply glass/epoxy doublers as a way to prevent the deflection of the specimens during the DCB test. While this can be an effective method of reducing the deflection, it can also increase the overall fracture toughness of the specimen, since when solicited, damage can develop at interfaces between the doublers and the specimen which dissipates fracture energy. This circumstance leads to erroneous estimations of material fracture toughness, which is difficult to keep account. Even if this type of over estimation can be made negligible by considering the use of a strong adhesive, it must be taken into account that there is no reference for the expected fracture toughness values of the specimens, which makes difficult the assessment of the relevance of spurious energy being dissipated. For these reasons, another approach was followed based on dimensioning of specimens taking into consideration the low Young modulus (E_1) of the material. The bending stiffness ($E_1 * I$) imposed for the specimen's arms was based on previous works [17,10] using DCB tests which have pointed to values of the order of 10^6 N/mm². Another condition was imposed, which was the specimen standards for the dimensioning presented in [12]. For the materials used, Nylon FX256 (PA12) and Nylon CF15 Carbon (PA12 + sCF), the mechanical property values were obtained from previously performed tensile tests on specimens created by the same FFF equipment and settings used to produce the DCB samples. For fully dense, $\pm 45^\circ$ infill, ISO 527 dogbones presented an average Young modulus for PA12 of 1564.6 ± 20.4 MPa, and for the PA12 + sCF, 1907.4 ± 98.7 MPa. In both cases, the specimen arms are thick balanced laminates and the propagation is mainly resin controlled at the pre-cracked interface. These conditions minimize the presence of spurious modes of loading (mode II and mode III) thus leading to predominant mode I [18,19]. From the array of combinations obtained, the decision on the final dimensions was also made based on the possible warping effect which can take place due to the thermal gradient induced by the continuous depositing of filament. The defined specimen dimensions were then obtained, being presented in Table 1 with the schematic representation in Fig. 2.

2.2.2. DCB printing strategy and production settings

The DCB specimens were manufactured accordingly the dimensions shown in Table 1, following a methodology for pre-crack creation iteratively developed. In order to match the mechanical properties obtained via tensile tests, ensuring the bending stiffness and toughness

Table 1
Specimen nominal dimensions.

Specimen Material	Length L [mm]	Width B [mm]	Height h [mm]	E_1 [MPa]	I [mm ⁴]	Pre-crack a_0 [mm]	$E_1 \cdot I$ [N*mm ²]
PA 12 + sCF	125	25	6	1907.4 \pm 98.7	450	50	8.5x10 ⁵
PA 12	115	25	6	1564.6 \pm 20.4	450	40	7.0x10 ⁵

needed for a correct crack propagation, 100% dense infill was used, also minimizing the part voids presence. For the production process, a commercially available Tronxy X5 3D printer from Shenzhen Tronxy Technology Co. Ltd was used, in which the extrusion process was performed with 0.4 mm diameter stainless steel nozzle, layer height of 0.3 mm and raster orientation $\pm 45^\circ$. Considering process temperatures, an extrusion temperature of 260 °C and a print bed temperature 90 °C were utilized. As a consequence of the high infill percentage applied, the amount of deposited material in each layer and the time needed to complete it also increases. This heavily influences the thermal gradient of the specimen, leading to a higher warping effect. In addition, another issue was found while printing the specimens, being it when creating the pre-crack during the printing. A Kapton® film was applied between the layers adjacent to the mid-plane of specimen. Being the specified height for each layer of the specimen 0.3 mm, the specimen then contains 40 separate layers, corresponding to its total height of 12 mm, which means the film is applied between the 20th and 21st layers. However, due to the inexistence of adhesion between the newly deposited layer and the Kapton® film, this process was not straightforward. Several attempts were performed in order to be able to insert the Kapton® film without affecting the printing of the specimen. In order to solve this problem, a new geometry was created, containing a disposable part solely for the film support, which was used to prevent the film and specimen from warping, by depositing 2 extra layers on top of the film. Also, the increase in adhering area to the heated bed is also beneficial since it counteracts the thermal contraction effect. The appearance of the new geometry is shown on Fig. 3a, and it consists in three different parts combined. The printing starts with parts (1) and (2) representing the support structure and DCB specimen which are both printed until reaching the height of 6 mm, and at this point the print is paused and the Kapton® film is applied in order to create the pre-crack, continuing with the enclosing layers (3) and the rest of the sample (2). This allows the Kapton® film to be sealed, while also preventing the layers deposited on top of it from warping, since part 3 also adheres to a part of the support which is not covered by the Kapton® film. After the printing job, the resulting part is taken out of the bed, and the support and film are cutted out, originating on a DCB specimen. Two piano hinges were bonded to the end of each specimen, following the procedure presented in the ASTM D5528 [20]. Prior to bonding, the surfaces of the hinges and the specimens were smoothed with sandpaper and cleaned with isopropyl alcohol to ensure the load transfer without debonding. After the application of the adhesive, a clamp was

placed in each specimen, as seen in Fig. 4, to prevent the hinges from moving and to guarantee an optimal cure process of the adhesive, which lasted 48 h.

Following this methodology, the production process, took approximately 2 h and 20 min for each sample. Table 2 presents the real dimensions of the created samples.

2.3. Testing procedure

After the completion of the cure process, the specimens were tested using an Instron Model 4208 universal testing machine with 5kN load capacity and an opening rate of 5 mm/min at environment temperature ($\approx 25^\circ\text{C}$). From Fig. 4 it is possible to understand that for both PA12 and PA12 + sCF crack propagation at the pre-cracked plane was able to be achieved, however it is distinguishable in between (a) and (b) the difference in flexibility. Since both samples have the same geometry, this is due to an inferior Young modulus for the unreinforced material.

2.4. Data reduction scheme

An equivalent crack length based procedure was followed to get the *Resistance-curve* (*R-curve*) as a function of load-displacement data. This method is particularly advantageous since crack length monitoring is difficult to be performed with the required accuracy due to unstable crack growth, and accounts indirectly by the energy dissipated in the fracture process zone (FPZ) [21]. The method relies on specimen compliance ($C = \delta/P$) determined through Timoshenko beam theory which can be expressed as [17],

$$C = \frac{8a^3}{E_1 B h^3} + \frac{12a}{5B h G_{13}} \quad (1)$$

where E_1 and G_{13} are the material elastic properties, a the crack length and B and h specimen dimensions (Fig. 2). This equation can be solved aiming to get the equivalent crack length a_e as a function of the current compliance, C using the Matlab® software [21,17]. Combining the Irwin-Kies equation

$$G_I = \frac{P^2}{2B} \frac{dC}{da} \quad (2)$$

with Eq. (1), yields

$$G_I = \frac{6P^2}{B^2 h} \left(\frac{2a_e^2}{h^2 E_1} + \frac{1}{5G_{13}} \right) \quad (3)$$

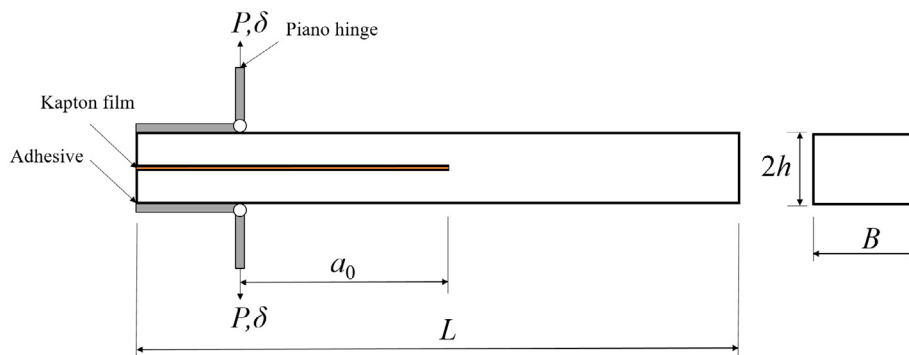


Fig. 2. DCB schematic representation.

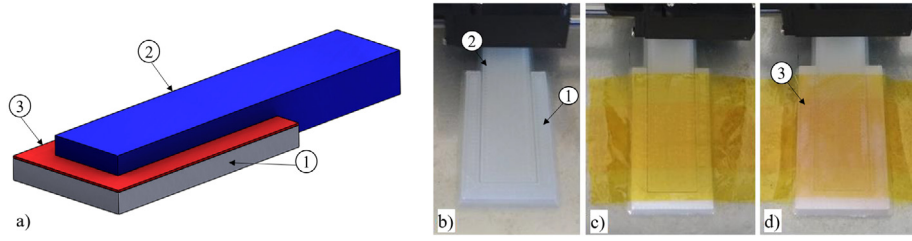


Fig. 3. (a) CAD model for the newly developed approach, (b) Support and specimen until 6 mm in height, (c) Kapton® film application and (d) Support enclosing layers and rest of the test sample.

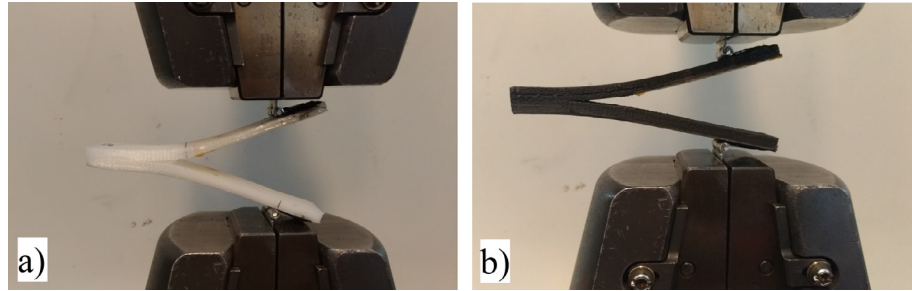


Fig. 4. DCB test at the end positions for: (a) PA 12 (b) PA 12 + sCF.

Table 2
Real specimen dimensions.

Specimen	Length L [mm]	Width B [mm]	Height h [mm]	Pre-crack a_0 [mm]
PA12-1	123.4	25.1	5.51	46.3
PA12-2	124.5	25.2	5.57	47.4
Average	123.9	25.1	5.54	46.9
St. Dev.	0.8	0.1	0.04	0.8
PA12-3	114.0	25.7	5.54	37.5
PA12 + sCF-1	114.9	25.8	5.58	37.6
PA12 + sCF-2	114.5	25.7	5.61	37.7
PA12 + sCF-3	115.5	25.7	5.51	37.2
Average	115.0	25.7	5.57	37.5
St. Dev.	0.5	0.1	0.05	0.2

Following this procedure, an estimation of the mode I energy release rate G_I as a function of the equivalent crack length a_e (R -curve) can be obtained, only requiring the data ensuing from the load-displacement curve. The only issues faced when applying this data reduction scheme were the values used for E_I , the Young modulus, and G_{13} , the shear modulus, which were not available. The Young modulus was determined by an inverse procedure fitting the initial stiffness of the numerical load-displacement curve to the experimental observed one. In order to get accurate values, each specimen was simulated considering its real dimensions instead of the nominal ones. In the case of the shear modulus, it can be observed from Eq. (3) that its importance is quite low when regarding the overall result. Consequently, a typical value was assumed for it, considering that in a generic orthotropic material the shear modulus is typically ten times lower than the Young modulus, for the referred direction.

3. Numerical analysis

Finite element analyses considering cohesive zone modelling (CZM) were performed aiming to identify softening laws representative of fracture behavior of the tested materials. These models allow reproducing material fracture behavior assuming two distinct stages. Before the occurrence of any damage, the model is in the linear elastic regime, being characterized by the following equation,

$$\sigma = E\delta_r \quad (4)$$

in which σ and δ_r are the stress and relative displacements vectors that develop between homologous points belonging to the surfaces of the cohesive element, and E is a diagonal matrix containing the interface stiffness. The values inputted in this matrix aim to satisfy two requirements: first, the value should be as high as possible in order to minimize unwanted interpenetrations when compression occurs [21]; second, the value is limited in order to avoid numerical problems. These circumstances led to a compromise giving rise to a value normally in the range $10^6 - 10^7$ N/mm³, usually known as the penalty parameter. After reaching the local strength, damage occurs, and the Eq. (4) turns into

$$\sigma = (I - D)E\delta_r \quad (5)$$

where I is the identity matrix, and D is a diagonal matrix containing the damage parameter, d , which is function of the softening law utilized. Two different cohesive laws were considered in this work, the trapezoidal and the trilinear one. In both cases, inverse procedures were used to identify the cohesive law (CL) representative of the material fracture behaviour. The CL is iteratively adjusted aiming a good fitting between the numerical and experimental load-displacement curves.

3.1. Trapezoidal cohesive law

The trapezoidal law is particularly adequate when non-linear fracture behaviour is present, thus being appropriate for PA12 whose load-displacement curves revealed some non-linearity after the peak load. This behavior is a symptom that some plasticity is associated to the fracture process, which is properly accounted for in the trapezoidal law (Fig. 5).

In the plateau region ($\delta_{1,I} \leq \delta_1 \leq \delta_{2,I}$) the damage parameter becomes,

$$d = 1 - \frac{\delta_{1,I}}{\delta_1} \quad (6)$$

being δ_1 the current relative displacement and $\delta_{1,I}$ obtained from the local cohesive strength σ_U and the initial stiffness value. The size of the plateau is given by $\delta_{2,I}$ and governs the plastic behaviour associated to fracture. After the second inflexion point ($\delta_{2,I}, \sigma_U$) a linear stress softening occurs till complete failure ($\delta_{2,I} \leq \delta_1 \leq \delta_{u,I}$) by means of the following damage parameter,

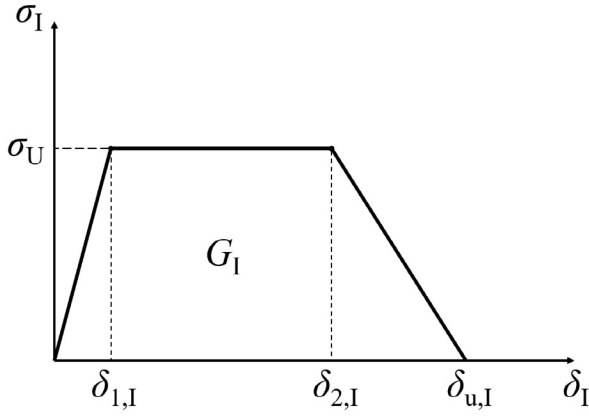


Fig. 5. Trapezoidal constitutive law for pure-mode I.

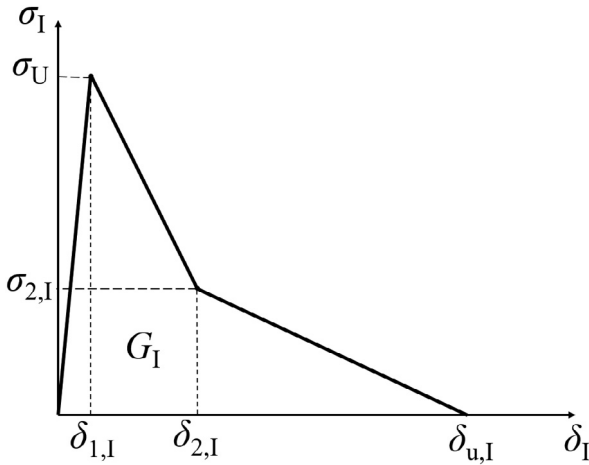


Fig. 6. Bilinear stress-softening constitutive law for pure-mode I.

$$d = 1 - \frac{\delta_{1,I}(\delta_{u,I} - \delta_I)}{\delta_I(\delta_{u,I} - \delta_{2,I})} \quad (7)$$

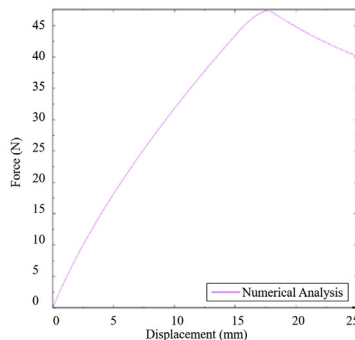
The ultimate relative displacement value $\delta_{u,I}$ is obtained equating the area of the trapezoid to the critical strain energy release rate,

$$\delta_{u,I} = \frac{2G_{Ic}}{\sigma_u} - \delta_{2,I} + \delta_{1,I} \quad (8)$$

In this case, the iterative procedure involves alteration of the parameters $\delta_{2,I}$ and σ_u till good agreement is achieved.

3.2. Trilinear cohesive law

This law is characterized by a bilinear softening relationship thus

Fig. 7. $P - \delta$ curve and corresponding state of the numerical DCB specimen at post peak zone.

being suitable for materials revealing different fracture mechanisms ahead of the crack tip, as is the case of micro-cracking and fiber bridging [21]. This fracture behaviour usually reflects on remarkable non-linearity of the load-displacement curves before the peak load (Fig. 6), which was observed in the PA12 + sCF material.

In the first softening branch ($\delta_{1,I} \leq \delta_I \leq \delta_{2,I}$) the damage parameter writes,

$$d = \frac{\delta_{2,I}(\delta_I - \delta_{1,I})(1 - \phi)}{\delta_I(\delta_{2,I} - \delta_{1,I})}, \quad \delta_{1,I} \leq \delta_I \leq \delta_{2,I} \quad (9)$$

being $\phi = (\sigma_{2,I} \cdot \delta_{1,I}) / (\sigma_U \cdot \delta_{2,I})$. For the final branch the damage parameter yields

$$d = 1 - \frac{\phi \delta_{2,I}(\delta_{u,I} - \delta_I)}{\delta_I(\delta_{u,I} - \delta_{2,I})}, \quad \delta_{2,I} \leq \delta_I \leq \delta_{u,I} \quad (10)$$

where the ultimate displacement $\delta_{u,I}$ is given by the area under the stress-relative displacement softening model,

$$\delta_{u,I} = \frac{2G_{Ic} + \sigma_{2,I}\sigma_{1,I} - \sigma_{u,I}\delta_{2,I}}{\delta_{2,I}} \quad (11)$$

In this model, an additional parameter ($\sigma_{2,I}$) is included in the inverse procedure in order to fit the numerical and experimental load-displacement curves.

3.3. Finite element analysis

The models described earlier were implemented as a user subroutine, in ABAQUS® software. Plane strain analysis was assumed, owing the width of the specimens, considering 8-node solid isoparametric rectangular elements with mesh refinement in the region where crack propagation occurs, aiming to get more accuracy. The cohesive zone, where damage is susceptible to occur (the mid-plane of the specimen), was modelled by 106 6-node cohesive elements compatible with the solid elements as seen in Fig. 7.

4. Results and discussion

The experimental load-displacement curves were registered in the course of the DCB tests. Subsequently, the data reduction scheme described in Section 2.4 was applied aiming to get the corresponding resistance-curves. The critical strain energy release rate was obtained from the plateau region of these curves and used as input in the numerical analysis in order to determine cohesive laws representative of materials fracture behaviour. Three experimental results were obtained for each material.

4.1. Nylon FX256 (PA12)

Figs. 8 shows the experimental load-displacement curves and the corresponding R-curves obtained for PA12. It can be observed that after

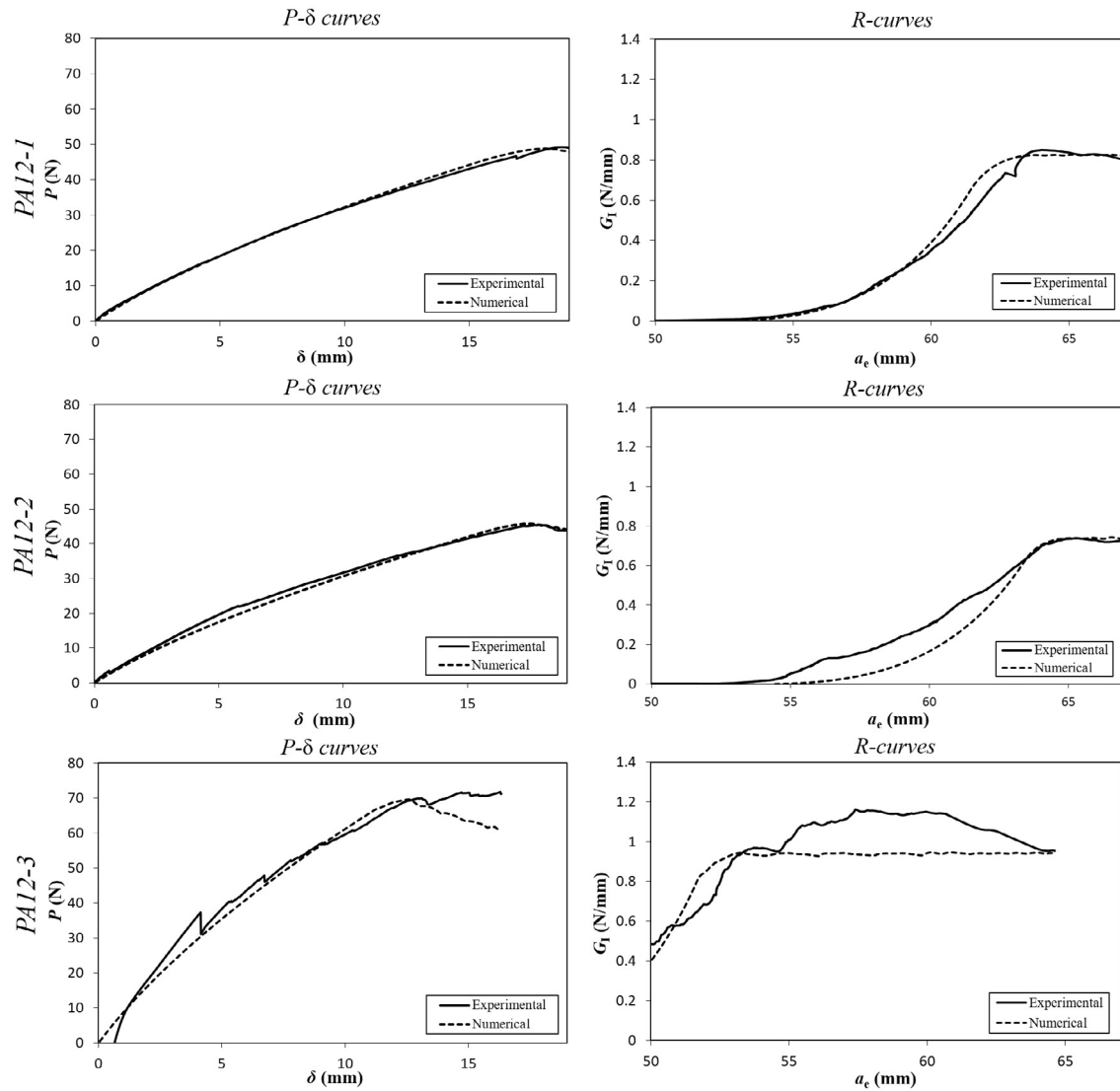


Fig. 8. $P - \delta$ and the corresponding R -curves of DCB PA12 tests.

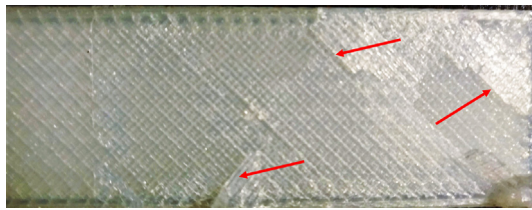


Fig. 9. Fractured surfaces after the DCB test for a PA12 specimen (arrows evidence pull out layer).

Table 3

Cohesive parameters obtained for PA12 specimens.

Specimen	σ_u [MPa]	$\delta_{2,I}$ [mm]	G_{Ic} [N/mm]
PA12-1	0.48	1.35	0.81
PA12-2	0.45	1.38	0.73
PA12-3	0.75	1.00	0.86
Average	0.56	1.24	0.80
CoV [%]	29.5	17.0	8.2

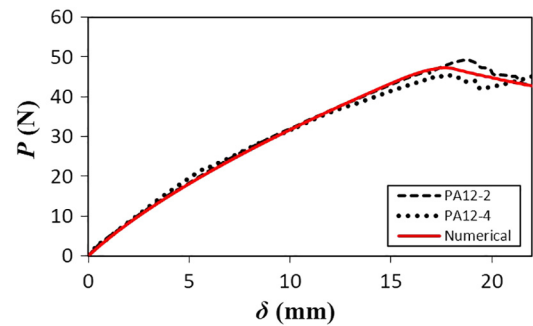


Fig. 10. Comparison of the numerical $P - \delta$ curve obtained with the average cohesive law with the experimental ones for PA12 considering a nominal $a_0 = 50$ mm.

peak load the load decreases smoothly meaning that nonlinear fracture phenomenon is occurring. Typically, the ensuing R -curves reveal two main regions. Initially, a gradual rising trend is observed until a plateau develops. The first branch corresponds to FPZ development and its large extension is a symptom of substantial FPZ, which reinforces the idea of a nonlinear fracture mechanics behaviour. Two initial tests with a nominal $a_0 = 50$ mm were performed. Since large displacements were

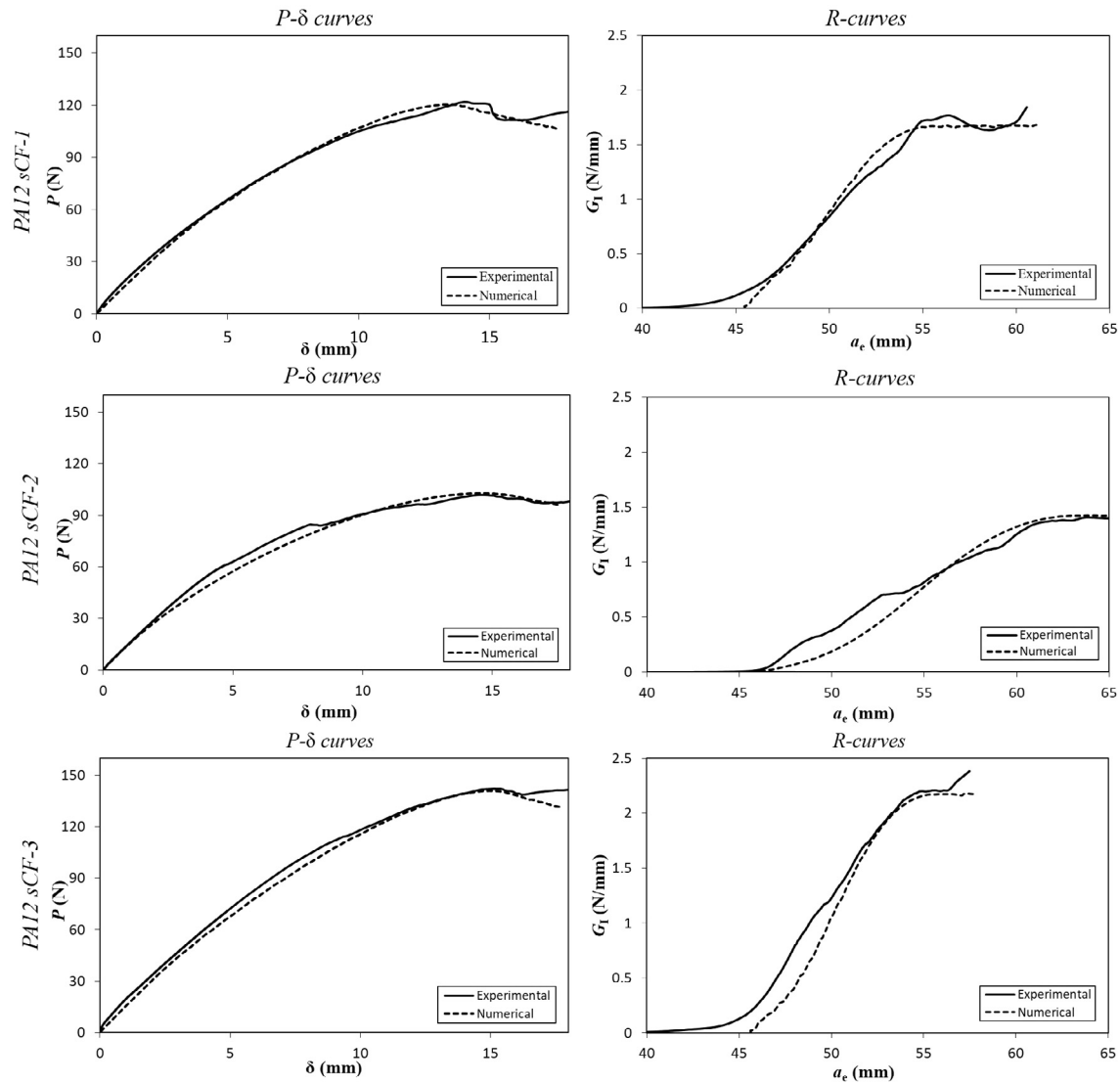


Fig. 11. $P - \delta$ and the corresponding R -curves of DCB PA12 sCF tests.

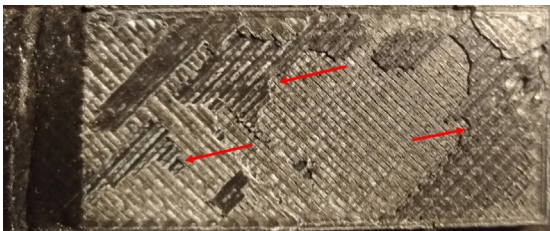


Fig. 12. Fractured surfaces after the DCB test for a PA12 + sCF specimen.

Table 4

Cohesive parameters obtained for the reinforced specimens.

Specimen	σ_u [MPa]	$\delta_{2,l}$ [mm]	$\sigma_{2,l}$ [MPa]	G_{Ic} [N/mm]
PA12 sCF-1	3.25	0.13	1.50	1.70
PA12-sCF-2	1.00	0.10	0.77	1.44
PA12-sCF-3	3.40	0.07	1.85	2.21
Average	2.55	0.10	1.37	1.78
CoV [%]	52.7	30.0	40.1	22.0

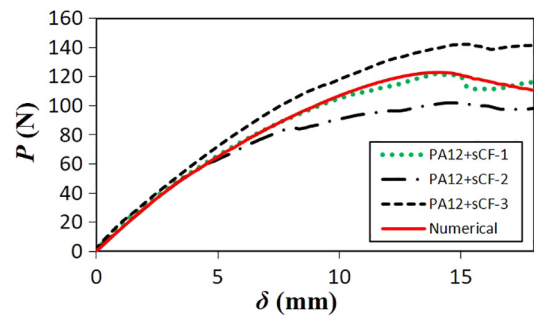


Fig. 13. Comparison of the numerical $P - \delta$ curve obtained with the average cohesive law with the experimental ones for PA12 considering a nominal $a_0 = 40$ mm for PA12 + sCF.

observed the third one was executed with a nominal $a_0 = 40$ mm. However, no remarkable influence of the initial pre-crack length or measured toughness was observed. In fact, the values of strain energy release rate of the three tests converge to values around 0.8 N/mm revealing consistency. It was observed that the trapezoidal law is appropriate to deal with fracture behavior of PA12. The inverse procedure originates numerical load-displacement and R -curves in agreement with

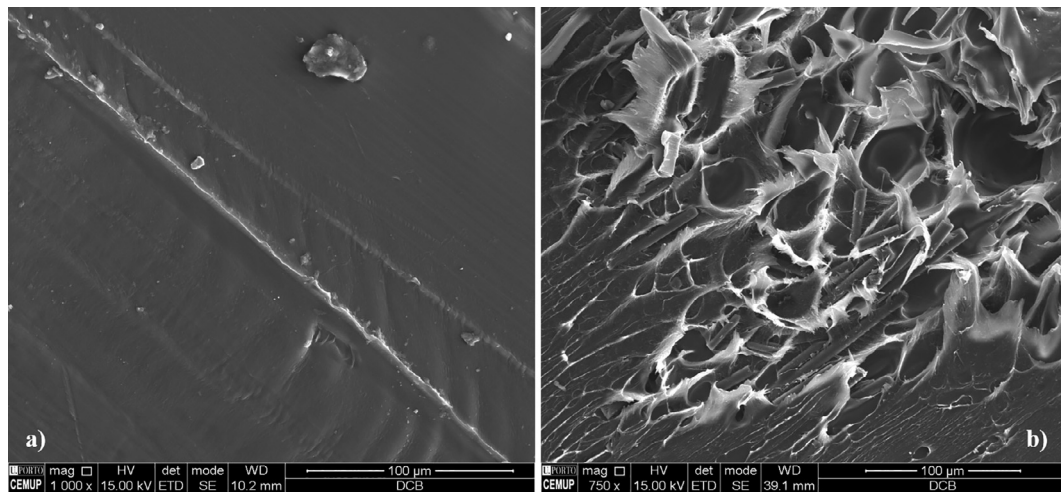


Fig. 14. Comparison of the fractured surfaces for the (a) unreinforced and (b) reinforced specimens.

the experimental ones (Figs. 8). The found discrepancies are due to spurious experimental effects related to pull-out layers occurring occasionally (Fig. 9), leading to the observed irregular pattern on load-displacement and R -curves.

Table 3 lists the cohesive parameters obtained for each specimen as well as the respective average values.

The average cohesive law was used to obtain a typical load-displacement curve of PA12 and the ensuing curve was compared in Fig. 10 with the experimental ones respecting to tests with a nominal $a_0 = 50$ mm. It can be concluded that the numerical $P - \delta$ curve reproduces the experimental ones, meaning that the obtained CL represents well the fracture behaviour of PA12.

4.2. Nylon CF15 Carbon (PA12 + sCF)

The experimental load-displacement curves and the respective R -curves of the three performed tests are plotted in Figs. 11. All the tests were executed with a nominal $a_0 = 40$ mm owing the statement that much higher toughness was obtained when compared to PA12. In fact, higher initial pre-racks would lead to unwanted quite large displacements. The initial stiffness increased markedly (approximately twice) relative to unreinforced material; the longitudinal elastic modulus (E_1) obtained by an inverse procedure points to 2973 MPa instead of the 1474 MPa found for PA12.

Characteristically, the load-displacement curves revealed a pronounced non-linear behaviour before peak load is attained, which makes more adequate the trilinear CL with bilinear softening relationship. Although the phenomenon of pull-out layers leading to sporadic intralaminar failure is also present in this material (Fig. 12), its effect on irregular pattern of experimental curves is less pronounced. Overall, good agreement was achieved in load-displacement as well as in R -curves, proving the appropriateness of the trilinear cohesive law to reproduce fracture behaviour of PA12 + sCF.

The cohesive parameters are listed in Table 4. Although some scatter can be observed, a special remark should be pointed concerning the high value of G_{ic} comparatively to PA12. The average values were used as input in a numerical simulation and the resulting $P - \delta$ curve replicates the overall trend of the experimental ones (Fig. 13).

4.3. Scanning electron microscopy (SEM) analysis

For a better understanding of the behaviour differences observed for each type of material and test, a SEM analysis was conducted. Fig. 14 shows the resulting surfaces of each type of material. Overall, it is possible to observe that the reinforced specimen exhibits an irregular

surface while on the other hand the unreinforced displays a much smoother one. The presence of fibres in fractured surface of reinforced specimen indicates that the fibres were effectively loaded during the test, which explains the higher fracture toughness of PA12 + sCF relatively to PA12.

5. Conclusions

Interlaminar fracture characterization under mode I loading of FDM printed components fracture was studied in this work. Double cantilever beam (DCB) tests were performed considered unreinforced (PA12) and reinforced materials (PA12 + sCF) and a suitable data reduction scheme based on equivalent crack length method was applied. In spite of some scatter, it was verified that reinforcing fibres contributes to increase markedly material toughness. A scanning electron microscopy (SEM) was performed and it was concluded that fibres were effectively loaded during the test, thus explaining the higher fracture toughness. A finite analysis including cohesive zone modelling was performed aiming to determine cohesive laws (CL) representative of the fracture behaviour of both materials. An inverse procedure was followed by iteratively adjusting the cohesive parameters in order to get numerical load-displacement curves in agreement with the experimental ones. It was concluded that the trapezoidal and trilinear CL are appropriate for PA12 and PA12 + sCF, respectively. In fact, the average cohesive laws were used in numerical simulations and the ensuing load-displacement curves were compared with the experimental ones. In both cases it was concluded that resulting numerical load-displacement curve replicates the overall trend of the experimental ones. The average toughness values obtained in this work for the two materials deserve a special comment. In fact, it is verified that these materials reveal a quite low cohesive strength and Young modulus when compared with traditional composites. However, a special remark should be done about the fracture toughness under mode I loading, whose values are in the range of 0.8–1.8 N/mm. These values are much higher than the ones of typical thermoset composites, usually in the range of 0.3–0.5 N/mm [22]. This reveals that these materials have a potential of application, namely when interlaminar fracture behaviour under mode I loading is a crucial design parameter to take into account.

Acknowledgements

Authors gratefully acknowledge the funding of Project: POCL-01-0145 -FEDER-016414, cofinanced by COMPETE 2020 and LISBOA 2020, through Fundo Europeu de Desenvolvimento Regional (FEDER) and by National Funds through Funda para a Cincia e Tecnologia (FCT);

of Project NORTE-01-0145-FEDER-000022 - SciTech - Science and Technology for Competitive and Sustainable Industries, cofinanced by Programa Operacional Regional do Norte (NORTE2020), through Fundo Europeu de Desenvolvimento Regional (FEDER). The third author acknowledges the Laboratrio Associado de Energia, Transportes e Aeronautica (LAETA) for the financial support by the project UID/EMS/50022/2013.

References

- [1] Ahn S-H, Montero M, Odell D, Roundy S, Wright PK. Anisotropic material properties of fused deposition modeling ABS. *Rapid Prototyping J.* 2002;8(4):248–57. <https://doi.org/10.1108/13552540210441166>.
- [2] Chin Ang K, Fai Leong K, Kai Chua C, Chandrasekaran M. Investigation of the mechanical properties and porosity relationships in fused deposition modelling fabricated porous structures. *Rapid Prototyping J.* 2006;12(2):100–5. <https://doi.org/10.1108/13552540610652447>.
- [3] Masood SH, Mau K, Song W. Tensile properties of processed FDM polycarbonate material. *Mater. Sci. Forum* 2010;654–656:2556–9. <https://doi.org/10.4028/www.scientific.net/MSF.654-656.2556>. URL: <http://www.scientific.net/MSF.654-656.2556>.
- [4] Ziemian S, Okwara M, Ziemian CW. Tensile and fatigue behavior of layered acrylonitrile butadiene styrene. *Rapid Prototyping J.* 2015;21(3):270–8. <https://doi.org/10.1108/RPJ-09-2013-0086>. URL: <http://www.emeraldinsight.com/doi/abs/10.1108/RPJ-09-2013-0086>.
- [5] Sood AK, Ohdar RK, Mahapatra SS. Improving dimensional accuracy of Fused Deposition Modelling processed part using grey Taguchi method. *Mater. Des.* 2009;30(10):4243–52. <https://doi.org/10.1016/j.matdes.2009.04.030>.
- [6] Santana L, Lino Alves J, da Costa Sabino A. Netto A study of parametric calibration for low cost 3D printing: Seeking improvement in dimensional quality. *Mater. Des.* 2017;135:159–72. <https://doi.org/10.1016/j.matdes.2017.09.020>.
- [7] Peng A, Xiao X, Yue R. Process parameter optimization for fused deposition modeling using response surface methodology combined with fuzzy inference system. *Int. J. Adv. Manuf. Technol.* 2014;73(1–4):87–100. <https://doi.org/10.1007/s00170-014-5796-5>. URL: <http://link.springer.com/10.1007/s00170-014-5796-5>.
- [8] Young D, Wetmore N, Czabaj M. Interlayer fracture toughness of additively manufactured unreinforced and carbon-fiber-reinforced acrylonitrile butadiene styrene. *Additive Manuf.* 2018;22(November 2017):883–90. <https://doi.org/10.1016/j.addma.2018.02.010>. URL: <https://doi.org/10.1016/j.addma.2018.02.023>.
- [9] in Park S, Watanabe N, Rosen DW. Estimating failure of material extrusion truss structures based on deposition modeling and a cohesive zone model. *Mater. Des.* 2018;147:122–33. <https://doi.org/10.1016/j.matdes.2018.03.034>.
- [10] Spoerk M, Arbeiter F, Cajner H, Sapkota J, Holzer C. Parametric optimization of intra- and inter-layer strengths in parts produced by extrusion-based additive manufacturing of poly(lactic acid). *J. Appl. Polym. Sci.* 2017;134(41):1–15. <https://doi.org/10.1002/app.45401>.
- [11] Islam MS, Prabhakar P. Interlaminar strengthening of multidirectional laminates using polymer additive manufacturing. *Mater. Des.* 2017;133:332–9. <https://doi.org/10.1016/j.matdes.2017.07.038>.
- [12] ASTM International, Standard Test Method for Mode I Interlaminar Fracture Toughness of Unidirectional, West Conshohocken, PA, 2013, www.astm.org 01 (Reapproved 2007) (2013) 1–12. doi:10.1520/D5528-01R07E03.2.
- [13] Zhang W, Cotton C, Sun J, Heider D, Gu B, Sun B, et al. Interfacial bonding strength of short carbon fiber/acrylonitrile-butadiene-styrene composites fabricated by fused deposition modeling. *Compos. Part B: Eng.* 2018;137(August 2017):51–9. <https://doi.org/10.1016/j.compositesb.2017.11.018>.
- [14] C. Ziemian, M. Sharma, S. Ziemian, Anisotropic Mechanical Properties of ABS Parts Fabricated by Fused Deposition Modelling, *Mechanical Engineering* arXiv:0803973233, doi:10.5772/34233.
- [15] Aliheidari N, Christ J, Ameli A, Tripuraneni R, Nadimpalli S. Measuring the inter-layer fracture resistance of FDM printed thermoplastics. *SPE ANTEC Indianapolis* 2016:5–9.
- [16] Tymrak BM, Kreiger M, Pearce JM. Mechanical properties of components fabricated with open-source 3-D printers under realistic environmental conditions. *Mater. Des.* 2014;58:242–6. <https://doi.org/10.1016/j.matdes.2014.02.038>. arXiv:arXiv:1011.1669v3.
- [17] Dias GF, de Moura MF, Chousal JA, Xavier J. Cohesive laws of composite bonded joints under mode I loading. *Compos. Struct.* 2013;106:646–52. <https://doi.org/10.1016/j.compstruct.2013.07.027>.
- [18] De Morais AB, De Moura MF, Gonçalves JP, Camanho PP. Analysis of crack propagation in double cantilever beam tests of multidirectional laminates. *Mech. Mater.* 2003;35(7):641–52. [https://doi.org/10.1016/S0167-6636\(02\)00289-2](https://doi.org/10.1016/S0167-6636(02)00289-2).
- [19] Samborski S. Numerical analysis of the DCB test configuration applicability to mechanically coupled Fiber Reinforced Laminated Composite beams. *Compos. Struct.* 2016;152:477–87. <https://doi.org/10.1016/j.compstruct.2016.05.060>.
- [20] A.D 5528-94a, Standard test method for mode I interlaminar fracture toughness of unidirectional fiber-reinforced polymer matrix composites, *Tech. rep.*, ASTM (1994).
- [21] de Moura MF, Morais JJ, Dourado N. A new data reduction scheme for mode I wood fracture characterization using the double cantilever beam test. *Eng. Fract. Mech.* 2008;75(13):3852–65. <https://doi.org/10.1016/j.engfracmech.2008.02.006>.
- [22] de Morais A, Pereira A, de Moura M, Silva F, Dourado N. Bilinear approximations to the mixed-mode I-II delamination cohesive law using an inverse method. *Compos. Struct.* 2015;122:361–6. <https://doi.org/10.1016/j.compstruct.2014.11.058>. exported from <https://app.dimensions.ai> on 2018/10/30. <https://app.dimensions.ai/details/publication/pub.1048873712>.